Su et al. *NPG Asia Materials* (2024) 16:21
https://doi.org/10.1038/s41427-024-00539-7

NPG Asia Materials

ARTICLE Open Access

A bone adhesive enhances osteoporotic fracture repair by regulating bone homeostasis

Shenghui Su[1], Jiajun Xie[2], Jian Gao[2], Shencai Liu[2], Xieping Dong[3], Jianwei Li[4], Zhong Feng Gao[5], Keyuan Chen[6] and Weilu Liu[2]

Abstract

Patients suffering from osteoporotic fractures often require effective fixation and subsequent bone repair. However, the currently available materials are functionally limited and often fail to improve outcomes in this patient population. In this study, we developed orthopedic adhesives doped with romosozumab-loaded mesoporous bioactive glass nanoparticles to aid in osteoporotic fracture fixation and restore dysregulated bone homeostasis. These adhesives were designed to promote osteoblast formation while simultaneously inhibiting osteoclastic bone-resorbing activity, thus working synergistically to promote the healing of osteoporotic fractures. Orthopedic adhesives exhibit injectability, reversible adhesiveness, and malleability, enhancing their adaptability to complex clinical scenarios. Furthermore, the release of romosozumab from mesoporous bioactive glass nanoparticles accelerated osteogenesis and inhibited osteoclastogenesis, delaying the bone resorption process. This dual action contributes to the regulation of bone regeneration and remodeling. Notably, our orthopedic adhesive could restore the disrupted bone homeostasis associated with osteoporotic fractures.

Introduction

Osteoporosis has recently emerged as a prevalent and serious skeletal condition among elderly individuals and is attributed to a decrease in bone density and quality[1]. With the aging of the global population, this issue has become increasingly important. Projections for 2050 indicate that individuals aged 65 years and older will outnumber young adults aged 15 to 24 years, marking a pivotal demographic shift. As a result, an increasing share of healthcare resources will inevitably be allocated to managing conditions commonly found in this older population, notably osteoporosis and subsequent bone fractures[2]. The current treatment approach for osteoporotic fractures includes surgical intervention to stabilize fractures and pharmaceutical intervention to address the underlying osteoporosis. In the context of osteoporosis, early surgical intervention is often more efficient than conservative treatment is, yielding improved prognoses and reduced perioperative complications[3,4]. Pharmacotherapy targeting bone stability is often employed to decrease the failure rate of internal fixation in osteoporotic patients. However, notably, in vivo enzymatic breakdown or swift elimination of drugs by the kidneys necessitates the administration of high concentrations of drugs, which can result in unexpected costs, adverse systemic effects, or insufficient localized drug concentrations[5]. In this context, facilitating the fixation of osteoporotic fractures and correcting dysregulated bone homeostasis post-fracture fixation are pivotal for expediting osteoporotic fracture healing. Currently, materials capable of concurrently addressing these two pathological aspects while providing fracture fixation are lacking.

For comprehensive management of osteoporotic fractures, a well-engineered fixation device requires auxiliary fracture fixation capabilities in addition to the ability to

Correspondence: Zhong Feng Gao (chm_gaozf@ujn.edu.cn) or Keyuan Chen (chancoy@163.com) or Weilu Liu (liuweilu_123@163.com)
[1]Department of Orthopaedics, Ningde Municipal Hospital of Ningde Normal University, Ningde 352100, China
[2]Division of Orthopaedic Surgery, Department of Orthopaedics, Nanfang Hospital, Southern Medical University, Guangzhou 510515, China
Full list of author information is available at the end of the article
These authors contributed equally: Shenghui Su, Jiajun Xie, Jian Gao

© The Author(s) 2024
Open Access This article is licensed under a Creative Commons Attribution 4.0 International License, which permits use, sharing, adaptation, distribution and reproduction in any medium or format, as long as you give appropriate credit to the original author(s) and the source, provide a link to the Creative Commons licence, and indicate if changes were made. The images or other third party material in this article are included in the article's Creative Commons licence, unless indicated otherwise in a credit line to the material. If material is not included in the article's Creative Commons licence and your intended use is not permitted by statutory regulation or exceeds the permitted use, you will need to obtain permission directly from the copyright holder. To view a copy of this licence, visit http://creativecommons.org/licenses/by/4.0/.

restore dysregulated bone equilibrium (stimulating osteogenesis and inhibiting osteoclast activity). The use of an osteogenic adhesive as an adjunctive tool in osteoporotic fracture treatment has become popular for facilitating the fixation of intricate fragments[6]. These tissue adhesives have adaptable structures, innate self-adhesion, remarkable flexibility, and outstanding biocompatibility, making them well-suited for attachment to diverse tissues, particularly cartilage and bone interfaces[7–9]. Moreover, these materials can serve as carriers for therapeutic agents, thereby influencing the wound-healing process in addition to their adhesive and wound-sealing properties[10–12]. In addition to wound adhesion and sealing, these adhesives can also expedite healing by transporting therapeutic agents[7,8,13]. Hence, biomedical adhesive hydrogels show potential as novel therapeutic materials for facilitating fracture fixation and promoting healing through robust adhesion to fractured bones.

However, in contrast to normal bone fractures, restoring dysregulated bone equilibrium after osteoporotic fractures is equally important. In osteoporotic fractures, disrupted bone homeostasis, particularly disrupted osteoclast formation and bone resorption, leads to a diminished bone-forming capacity[3]. Osteoporotic fracture implants should mechanically stabilize fractures with appropriately matched support, promote osteogenesis, and suppress osteoclast formation to reinstate fracture homeostasis[14,15]. Sclerostin, a bone formation inhibitor, reportedly inhibits Wnt/β-catenin signaling, mitigating osteoblast production by orchestrating mesenchymal stem cell differentiation and enhancing osteoclast generation by reducing osteoprotegerin expression in osteoblasts and osteocytes[16,17]. These findings underscore the role of sclerostin in regulating bone homeostasis, given its potent osteoporotic activity[18,19]. Consequently, developing a medical bone adhesive that facilitates the restoration of dysregulated bone equilibrium and supports the healing of osteoporotic fracture fragments is important.

In this study, we designed a medical bone adhesive crosslinked with gelatin and oxidized chondroitin sulfate (OCS) that incorporated mesoporous bioactive glass nanoparticles (MBGNs) loaded with a sclerostin antibody (romosozumab). This construct, referred to as the Gel-OCS/romosozumab@MBGN hydrogel (GORoM-gel), is designed to immobilize fragmented fractures and inhibit sclerostin, thereby stimulating bone formation to enhance fracture healing in osteoporotic comminuted fractures. MBGNs promote bone regeneration and possess a high surface area, making them suitable nanocarriers for romosozumab[20]. An in vitro coculture system was used to assess the biocompatibility, adhesion, and viability of bone marrow mesenchymal stem cells (BMSCs) on the GORoM-gel (Fig. 1B). Furthermore, osteoporotic rat models with comminuted femur fractures were established to investigate the impact of GORoM-gel on the healing of osteoporotic comminuted fractures (Fig. 1A).

Materials and methods

Synthesis of OCS

For synthesis of 5 g of oxidized chondroitin sulfate, sodium periodate was used as previously described[21]. Sodium periodate ($NaIO_4$), a potent oxidizing agent, selectively reacts with the cis-diol functional groups on the sugar units of chondroitin sulfate. This reaction involves cleaving the carbon–carbon bond adjacent to the hydroxyl group, creating aldehyde groups. In brief, 5 g of chondroitin sulfate was dissolved in deionized water. Subsequently, 8 g of sodium periodate was introduced into the reaction mixture, ensuring a sufficient excess to achieve complete oxidation. The reaction occurred at room temperature. When the desired degree of oxidation was obtained, the reaction was stopped by the addition of ethyl alcohol. The resultant oxidized chondroitin sulfate was isolated through dialysis. Next, the dialysate was transferred into a 50 mL centrifuge tube, frozen for 1 day (at −20 °C), and subsequently subjected to freeze-drying using a freeze dryer (FD-10, China) for 7 days, resulting in the production of OCS powder.

Synthesis of MBGNs

MBGNs were synthesized by established methods that were previously reported[21]. Briefly, hexadecyl trimethyl ammonium bromide (CTAB, Aladdin, Shanghai) was dissolved in deionized water to yield a 132 mL solution with a concentration of 21.21 g/L (w/v), after which the mixture was stirred until complete dissolution. Then, 40 mL of ethyl acetate (EA, Aladdin) was added to the above solution, and the mixture was stirred for half an hour. Next, 14 mL of ammonia water (2 mol/L) was added. The above solution was stirred for 15 min before 14.40 mL of tetraethyl orthosilicate (TEOS, Aladdin) was added. After the solution was stirred for 30 min, 6.52 grams of calcium nitrate tetrahydrate (CN Aladdin) was added to the mixture. After 4 h of stirring, the gradual formation of colloids in solution resulted in a milky white appearance. The above colloidal solution was centrifuged at 8000 rad/s to obtain colloidal particles. The collected colloidal particles were washed three times with deionized water and then three times with ethanol. The collected colloidal particles were placed in a drying oven at 60 °C for one day and ground into a fine powder. Subsequently, the samples were gradually heated at a rate of 2 °C per minute until they reached 700 °C, at which point they were held for 3 h to eliminate organic materials and nitrates, resulting in the production of MBGNs.

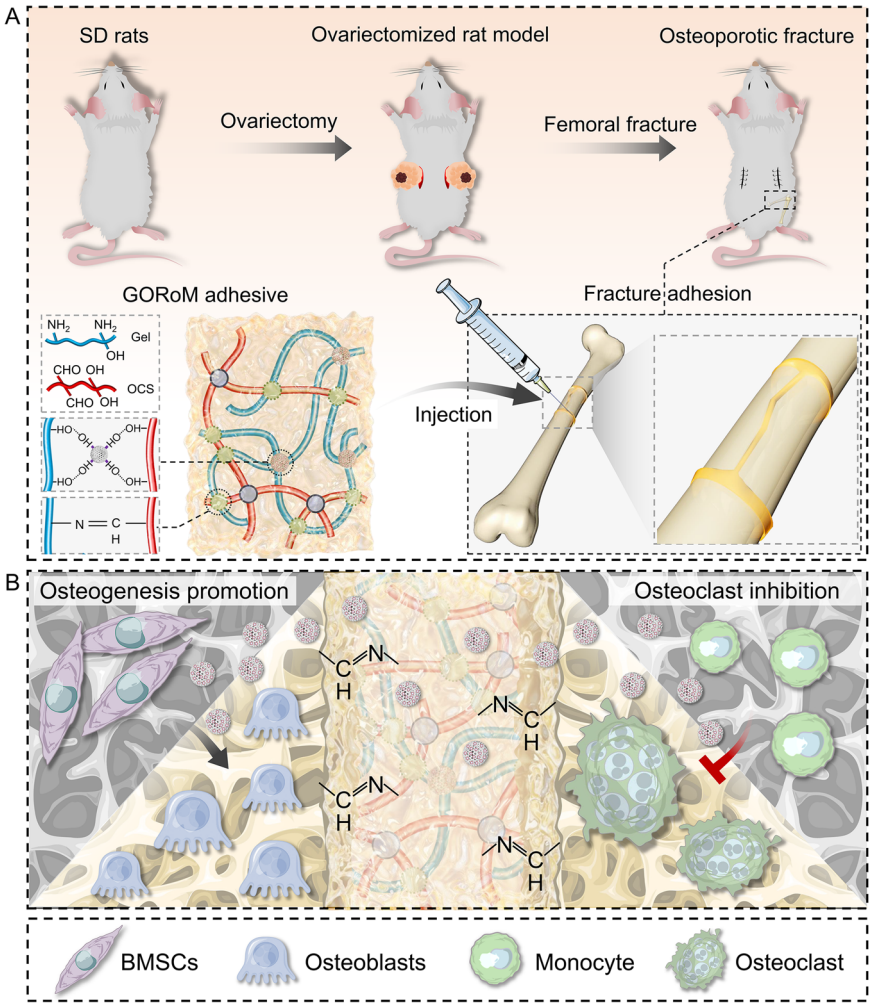

Fig. 1 Schematic diagrams of the GORoM adhesive and osteoporotic fracture treatment. A The process of OVX rat model establishment and GORoM adhesive implantation. **B** Osteoporotic fracture healing was mediated by osteogenic promotion and osteoclast inhibition.

Preparation of hybrid Gel-OCS/MBGNs/romosozumab hydrogels

The hybrid Gel-OCS/MBGNs/romosozumab hydrogels were prepared through a Schiff base reaction between gelatin and OCS. Initially, OCS was dissolved in deionized water at room temperature to produce an OCS solution with a specific concentration of 10% (w/v). Next, the MBGNs were introduced into a romosozumab solution at a specific concentration of 5% (w/v) to prepare romosozumab-loaded MBGNs (RoMs). The RoM suspension was carefully added dropwise into the OCS solution (5% v/v) and subjected to sonication, resulting in the formation of solution A. Then, solution B (a gelatin solution, 15% concentration) was prepared in deionized water and mixed with solution A while stirring to prepare hybrid Gel-OCS/MBGN/romosozumab (GORoM) hydrogels. The Gel-OCS (GO) hydrogel, Gel-OCS-romosozumab (GORo) hydrogel and Gel-OCS-MBGN (GOM) hydrogel were synthesized without the addition of RoM, MBGNs and romosozumab, respectively.

Characterization of the self-healing performance

During the experiment, the self-healing capability was assessed by splitting two adhesive materials into halves and then reassembling them following an exchange. After the samples were allowed to heal for 15 min, tensile stress was manually applied using tweezers.

Material characterization

As previously reported, field emission scanning electron microscopy (FE-SEM, Zeiss) was used to examine the internal structure and morphology of the hydrogels. The hydrogel samples were observed under FE-SEM after the samples had been lyophilized for three days. Transmission electron microscopy (TEM) was used to study the surface morphology of the MBGNs. A gold film was sputtered

onto all the samples (SC7620, Quorum Technologies, UK) for 60 s. An FTIR spectrometer from Thermo Fisher was used to analyze the chemical composition of the hydrogels. The GORoM hydrogels were analyzed by thorough grinding after lyophilization. A rheological test (Physica MCR301, Anton Paar) was carried out to measure the storage modulus (G') and loss modulus (G") of GORoM. A sample stage was used to place the GORoM hydrogels, and a diameter flatbed device was used to test them. At a strain amplitude of 5.0%, the frequency–modulus curves tested between 0.1 and 100 rad/s yielded the storage modulus (G′) and loss modulus (G") of the material. Confocal microscopy was used to detect the colocalization of the MBGNs (FITC staining) and romosozumab (rhodamine B staining) in the hydrogels.

Characterization of the physical properties of the adhesives

To assess the adhesive strength of GORoM, we conducted an experiment involving freshly cut bone segments affixed to a pig femur. A water-filled container was attached to the joint to evaluate its adhesive capacity, and the adhesive was allowed to solidify for one minute. Subsequently, the bonded bone segments were preconditioned overnight in a 37 °C PBS solution. During the tensile mechanical test, we measured the maximum tensile stress exhibited by the connected joint in both the end-to-end and lap-shear orientations using a Hengyi HY-1080 machine from Shanghai, China. Similar bone segments were connected in an end-to-end configuration to further assess adhesion and flexibility. Specifically, we forcibly separated two pairs of bone fragments treated with GORoM from their original positions and then recombined them.

Degradation rates of hydrogels in vivo and in vitro

We assessed the degradation rate of the GORoM-gel both in vitro and in vivo. For in vitro analysis, the gel was immersed in 5 ml of pH 7.4 PBS and continuously shaken at room temperature. The sample was washed and weighed every three days. For in vivo evaluation, 500 µl of the hydrogel was injected subcutaneously into rats. Observations were made on Days 0, 7 and 14 to comprehensively analyze the biodegradation behavior.

In vitro studies

Romosozumab release profile

The bicinchoninic acid (BCA) detection method was used to determine the daily and cumulative release profiles. For determination of the release profile of romosozumab from GOM, romosozumab and the GOM hydrogel were combined to produce the GORoM hydrogel. The GORoM mixture was incubated in PBS at 37 °C. On Days 1, 3, 7, and 14, the supernatant was collected for free romosozumab detection by BCA analysis.

Preparation of BMSCs and BMDMs

We obtained BMSCs from the bilateral humeri and femurs by rinsing the bone marrow cavity of female Sprague-Dawley (SD) rats (2 weeks old), as described in a previous study[22]. In addition, BMSCs were cultured in low-glucose DMEM supplemented with 10% fetal bovine serum (FBS; Gibco) at 37 °C with 5% CO_2. For rats aged four weeks, the femurs and tibias were removed, and bone marrow was extracted from the bones. For cell collection, the mixture was filtered using nylon mesh as a filtration medium and centrifuged for five minutes at 300 × g using nylon mesh as the top layer. The remaining cells were mixed in 1 mL of red blood cell lysis buffer, lysed at 4 °C for 10 min, washed with 1 mL of PBS to stop lysis, and centrifuged at 400 × g for 5 min. Complete medium containing M-CSF at a concentration of 100 ng/mL was used to stimulate monocytes from bone marrow cells to develop into macrophages.

In vitro biocompatibility testing

In vitro biocompatibility testing consisted of cell viability, proliferation, and adhesion experiments. BMSCs were seeded into 12-well culture plates at a density of 1×10^6 and were cocultured with each group of samples for 24 h for Live/Dead staining experiments. A total of 1×10^6 BMSCs were seeded on the surface of each group of samples for 1, 3, and 7 days. After coculture, CCK-8 solution (Beyotime) was added to each well. After 2 h, 100 µl of the supernatant in each well was transferred to a 96-well plate, and the absorbance was measured at 450 nm using a confocal microscope (BioTech).

Alkaline Phosphatase (ALP) staining

ALP activity was measured as follows: After 7 days of coculture of BMSCs with hydrogels, the culture medium was aspirated, and the cells were fixed with 4% paraformaldehyde for 30 min. The fixed samples were stained using an ALP dyeing kit (Beyotime), as recommended by the manufacturer. Images were taken using an inverted microscope (Nikon). The sample was then reacted with p-nitrophenylphosphoric acid, and the absorbance at 450 nm was measured using a microplate reader (Thermo Multiskan FC) to determine the amount of ALP.

Alizarin Red S (ARS) staining

After 14 days of coculture, the BMSCs with hydrogels were fixed in 4% paraformaldehyde for 30 min, after which 1% (w/v) ARS (pH 4.2; Sigma–Aldrich) was added to each well. After being washed three times with PBS following one hour of reaction, the samples were photographed. The mixture was kept at room temperature after

ARS was dissolved in 5% cetylpyridinium chloride (Sigma–Aldrich) in 10 mM sodium phosphate. Microplate readers (Thermo Multiskan FC) were used to measure the absorbance at 570 nm.

Gene expression

Total cellular RNA was extracted and reverse transcribed to cDNA using an RNA extraction and reverse transcription kit (Beyotime). PCR analysis was performed using LightCycler 480 SYBR Green Master Mix (TaKaRa). The reference gene GAPDH was used as an endogenous control. Determination of relative gene expression was calculated by the $2^{-\Delta Ct}$ method. Three independent experiments were carried out. The sequences of primers used in this study are listed in Table S1.

Western Blot

For protein extraction, cells were lysed at 4 °C with protein lysis buffer containing protease and alkaline phosphatase inhibitors. The total protein concentration was determined using a BCA kit (Beyotime). The first step in performing a Western blot was to separate the sample proteins based on their size using sodium dodecyl sulfate–polyacrylamide gel electrophoresis (SDS–PAGE). After electrophoresis, the proteins were transferred from the gel to polyvinylidene fluoride (PVDF, Thermo Fisher) membranes. Next, the membrane was blocked with nonfat dry milk. The primary antibodies (anti-OPN and anti-RunX2) were added and incubated overnight. Finally, the membrane was visualized using an enhanced chemiluminescence (ECL) agent (Abbkine).

In vivo studies

Rat osteoporotic femoral fracture model

A model of osteoporosis was established by removing the ovaries on both sides of 6-week-old female Sprague-Dawley (SD) rats. For determination of the effect of GORoM on the repair of osteoporotic comminuted fractures, the abovementioned osteoporotic rats were used to establish a femoral fracture model. After the femur was exposed, a comminuted fracture model was created in the mid-femur using a rongeur. After the fracture ends were connected with 1.2 mm diameter Kirschner wires, approximately 15 μl of GORoM was used to bind the fragments. In total, 18 SD rats were randomly divided into three groups ($n = 6$ each): the control group, the GO group, and the GORoM group. After 6 and 12 weeks, all the rats were sacrificed.

In vivo biocompatibility evaluation

Alanine aminotransferase (ALT), aspartate aminotransferase (AST), total protein (TP) and white blood cell (WBC) levels were determined after whole blood was collected from 12-week-old rats treated with materials to determine the in vivo biocompatibility. Hematoxylin-eosin (H&E) was used to stain the main organs, including the heart, lung, liver, spleen, and kidney.

Microcomputed tomography (Micro-CT) and histological analysis

A 4% paraformaldehyde solution was used to fix the femur samples. Micro-CT imaging of the specimens was performed using a SCANCO mCT50 at a scanning voltage of 70 kV, a scanning current of 200 A, and a resolution of 20 m. Microtomographic analysis software was used to construct 3D images. Materialize Mimics Research 19 software and a Hu value threshold of 600 to 1300 were used to quantify the volume of newly regenerated bone. Immediately after the micro-CT analysis, tissue samples were decalcified and dehydrated. H&E, Masson's trichrome, and immunohistochemical staining was performed on tissue sections sliced to a thickness of 10 mm using a rotary microtome (RM2255, Leica, Germany). For immunohistochemistry, anti-TRAP, Col-1, and OCN antibodies were used (Table S2). Photographs were taken with a microscope (Nikon, E800).

Statistical analysis

One-way analysis of variance (ANOVA) with Tukey's test was performed using GraphPad Prism 5. The experimental results are expressed as the mean ± standard deviation (mean ± SD). Each experiment was carried out at least three times. A P value < 0.05 was considered to indicate statistical significance.

Results and discussion

Preparation and characterization of GORoM hydrogel

For the fabrication of the GORoM hydrogel (Fig. 2A), OCS was synthesized based on a previously established protocol[21]. Fourier transform infrared (FTIR) analysis revealed the presence of a novel infrared band at 1725 cm^{-1} in the OCS spectra (Fig. 2B), which was attributed to the stretching vibration of aldehyde groups, confirming successful OCS oxidation. Subsequently, the MBGNs were synthesized following a previously outlined protocol[20]. Romosozumab was then loaded onto the MBGNs to create romosozumab-loaded MBGNs (RoM). At 37 °C, gelatin (30% (w/v)) and OCS (10% (w/v)) containing RoM (5% (w/v)) were combined to form the GORoM hydrogel. The interaction between the gelatin hydrogel skeleton's free amino group and the aldehyde group of OCS facilitated reversible covalent crosslinking through a Schiff base bond. Rheological analysis indicated that the storage modulus (G') of all three adhesives exceeded the loss modulus (G"), confirming their stability as viscoelastic solids[23]. Furthermore, no difference in the storage modulus was noted between the GOM and GORoM groups (2351 ± 20 vs. 2251 ± 50 Pa), underscoring that romosozumab did not

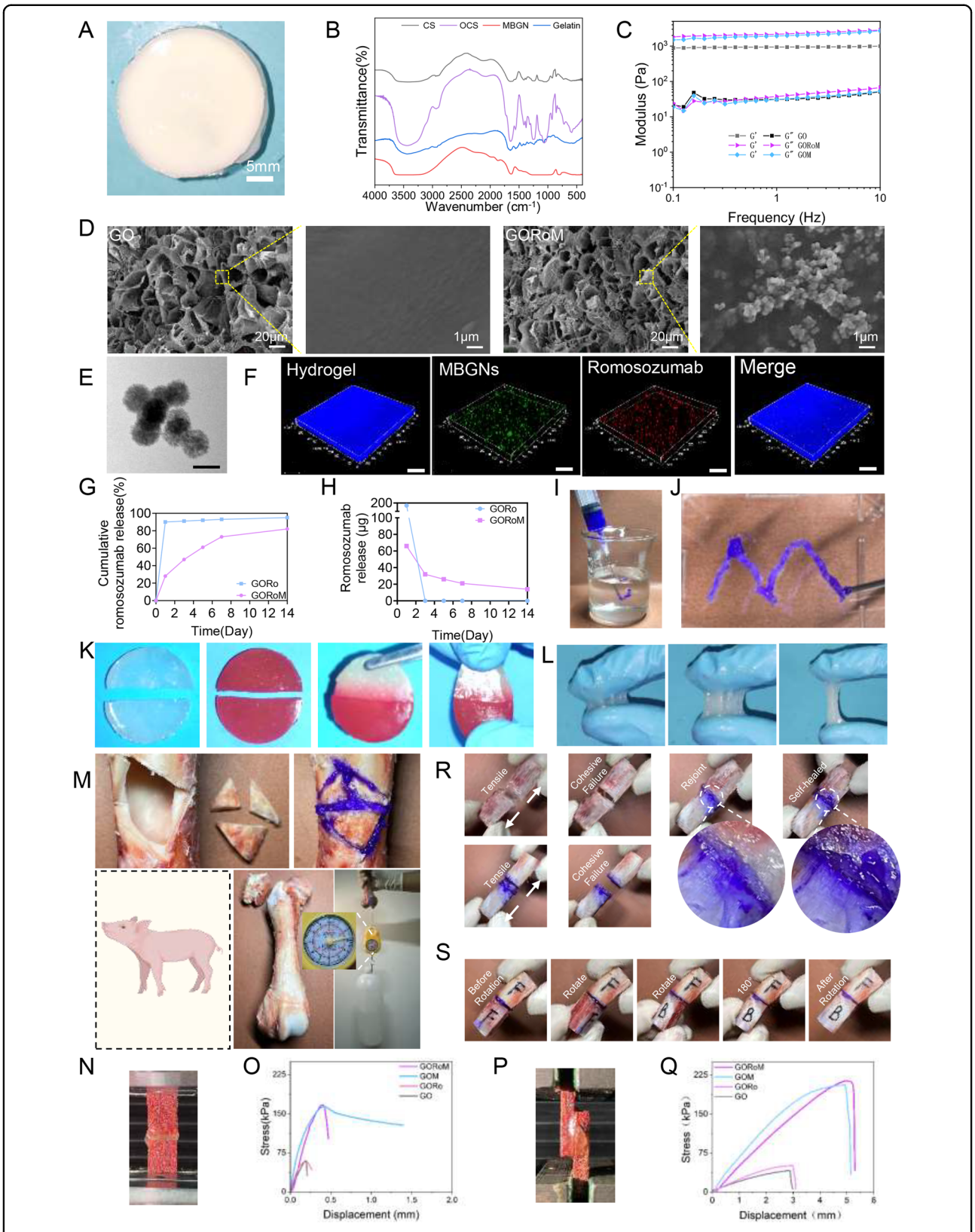

Fig. 2 (See legend on next page.)

(see figure on previous page)

Fig. 2 Crosslinking and physical properties of GO-based adhesives. A A physical image of the GORoM hydrogel (scale bar: 5 mm). **B** FTIR spectra of CS, OCS, MBGN, and gelatin. **C** Mechanical properties of GO, GOM, and GORoM. **D** The microstructures of the GO and GORoM hydrogels were observed via SEM. Scale bar: 20 μm and 1 μm. **E** TEM images (scale bar: 50 μm) of MBGNs. **F** Fluorescence images of labeled GORoM. Red, green, and blue indicate RhB-labeled romosozumab, FITC-labeled MBGNs, and DAPI-labeled gelatin, respectively. Scale bar: 100 μm. **G** The cumulative release profile of romosozumab with or without the GOM hydrogel after 14 days ($n = 3$). **H** The daily release curve of romosozumab with or without the GOM hydrogel ($n = 3$). **I** The GO-based adhesive can be smoothly injected into PBS to maintain a gel-like consistency. **J** The GO-based adhesive can be injected and used to write the letter "M". **K** Demonstration of the self-healing capacity of the hydrogels by cutting gelled GORoM hydrogels into halves and rejoining them to obtain healed interfaces. **L** The picture shows that the gelated GORoM hydrogel firmly adhered to the glove, demonstrating good adhesion. **M** Photographs showing that the GORoM hydrogel can be used to firmly resample freshly produced porcine-awed femur bone pieces, as evidenced by successful lifting of a 2.8 L water bottle. **N**, **O** Representative stress–displacement curve of the end–to-end tensile test. **P**, **Q** Representative stress–displacement curve of the lap-shear tensile test. **R** Reversible adhesiveness of the GORoM adhesive was demonstrated by rejoining and reconnecting breaking bone pieces. **S** Reversible adhesiveness of the GORoM adhesive was demonstrated by rotating one of the bonded bone pieces 180°.

influence the mechanical properties of the GOM hydrogel (Fig. 2C). SEM demonstrated the transparent porous structure of the hydrogel, with white MBGN particles distributed on the pore wall (Fig. 2D). This coarseness is attributed to the adherence of MBGNs, which contributes to a three-dimensional habitat that facilitates cell attachment, growth, and division. The porous structure of bioadhesive materials is integral to their design, enhancing their utility in osteoporotic fracture repair by improving their surface area, drug loading capacity, adhesive strength, and overall bone remodeling processes. Additionally, this structure has a specific effect on cellular activities. TEM highlighted the large surface area and mesoporous structure of the microspheres (Fig. 2E). The spatial distribution of romosozumab-loaded MBGNs within the hydrogel was revealed through three-dimensional immunofluorescence imaging (Fig. 2F). The biodegradability of the GORoM-gel was extensively evaluated. In vitro, the gel initially showed rapid degradation, with a significant reduction in mass within the first 14 days (Fig. S1A). In vivo observations mirrored this pattern, with a notable decrease in the gel bulk over time and minimal residue remaining by Day 14. These findings underscore the efficacious biodegradation of GORoM-gel both in vitro and in vivo (Fig. S1B). The degradation of the hydrogel can also be influenced by the concentration and release profile of bioactive substances, such as romosozumab, in the GOM hydrogel. The release of more than 80% of the loaded romosozumab over 14 days could affect the degradation rate of the hydrogel, initially causing rapid degradation both in vitro and in vivo. Collectively, these findings indicated the successful integration of romosozumab-loaded MBGNs into the GO hydrogel. Romosozumab release from the GOM hydrogel was sustained for more than 14 days, with more than 80% of the loaded romosozumab being released within this timeframe, ensuring substantial biological efficacy for fracture healing (Fig. 2G, H). Importantly, the GORoM hydrogel precursor exhibited excellent injectable properties, as it easily formed a stable gel when it was injected into water or into a petri dish using a syringe (Fig. 2I, J). The fracture repair ability of the adhesive was also demonstrated by splitting and reassembling the adhesive tablets (Fig. 2K). Finally, when applied to a gloved finger, the freshly prepared GORoM hydrogel adhered firmly to the glove surface (Fig. 2L). Collectively, these results validate the successful fabrication of the GORoM hydrogel.

Characterization of ex vivo adhesiveness to porcine bone

Effective tissue adhesiveness is critical for bone adhesives because it ensures swift and stable adherence to the defect site and facilitates cell recruitment for accelerated bone healing. The adhesiveness of the GO-based adhesives was assessed using fresh cancellous bone pieces from porcine femurs. The GORoM adhesive could rejoin bone fragments, as evidenced by its application to simple or severely comminuted fresh porcine femur fracture models (Fig. 2M). The reassembled freshly sawed porcine femur bone segments could even support the weight of a 2.8 L water bottle (Fig. 2M). While the GO hydrogel and GORo exhibited low adhesive strengths (58.3 ± 2.5 kPa and 59.1 ± 1.3 kPa for end-to-end, 40.2 ± 2.2 and 44.1 ± 3.6 kPa for lap-shear) before adhesive failure (Fig. 2N, O), both the GOM and GORoM hydrogels exhibited significantly greater adhesive strengths, exceeding 162 ± 5.6 kPa and 164.7 kPa ± 6.3 kPa for end-to-end tests (Fig. 2N, O), as well as 205.8 kPa ± 4.2 kPa and 213.3 kPa ± 7.1 kPa for lap-shear tests (Fig. 2P, Q), highlighting their excellent adhesive capabilities. In addition, we tested the effect of adding different concentrations of MBGNs on hydrogel stiffness, and the results showed that adding 10% MBGNs was the most appropriate treatment (Fig. S2). Incorporating 10% (w/v) MBGNs significantly improved the crosslinking density through physical and covalent mechanisms, enhancing the hydrogel's cohesion. Furthermore, Ca^{2+} released from the MBGNs facilitated Schiff base reactions at the adhesive-bone tissue interface, enhancing interfacial adhesion[24,25]. These findings demonstrated the suitability

of the GOM hydrogel for assisting in bone fracture fixation.

In addition to adhesive strength, flexibility is equally crucial. Adequate flexibility and adjustable adhesion provide surgeons with ample maneuvering space for aligning fracture fragments, which often requires numerous adjustments for optimal fracture reduction[26]. During demonstrations, we reconnected the broken pieces, rotated one segment by 180°, and reconnected the fragments (Fig. 2R). As the GORoM adhesive self-healed at the reconnected interface, the boundary between the fragments became indistinct, resulting in instant readhesion upon reassembly. Flexibility was further exemplified by rotating a reconnected bone segment by 180° (Fig. 2S). These results underscore the rapid self-healing ability of hydrogels prior to complete crosslinking, which relies on reversible intermolecular hydrogen bonding and dynamic covalent Schiff base networks. In summary, the flexibility and adjustability of these adhesives allow surgeons ample time for effective bone fragment reattachment.

In vitro and in vivo biocompatibility

Robust biocompatibility is imperative for bone adhesives. The survival, proliferation, and adherence of the GORoM hydrogel were assessed through the seeding of BMSCs onto hydrogel surfaces. These cell behaviors are pertinent to adhesive-bone integration and subsequent osteoporotic fracture healing. Live/Dead staining conducted one day after coculturing cells with hydrogels revealed a majority of live cells with green fluorescence (>90% cell viability) and a small number of red fluorescent dead cells (Fig. 3A). After 1, 3, and 7 days of coculture, the optical density values progressively increased due to cell proliferation, with no significant differences observed among the four groups (Fig. 3B). All the cells stained with *Amanita phalloides* exhibited distinct pseudopodia shapes with F-actin expression after 7 days of coculture (Fig. 3C). Furthermore, no significant difference in cell morphology was noted among the groups after 7 days of coculture. These observations corroborate the strong biocompatibility of each adhesive, indicating their safety for use.

In terms of in vivo biocompatibility, hydrogels from each group were subcutaneously injected into the backs of the rats. Histopathological analysis and organ-related blood tests (heart, liver, kidney, lung, and spleen) were used to evaluate the in vivo biocompatibility of each adhesive. Notably, no significant accumulation of hydrogel degradation products was found in the main organs of the rats, and no pathological abnormalities were observed (Fig. 3D). Moreover, the hydrogel groups exhibited no significant differences in the TP, ALT, AST or WBC levels compared to those of the control group (Fig. 3E), confirming the favorable in vivo biocompatibility of the hydrogel.

Osteogenic differentiation of BMSCs on GORoM

The dysregulation of bone homeostasis during osteoporosis, characterized by decreased bone-forming osteoblast activity and increased bone-resorbing osteoclasts, underscores the importance of re-establishing this balance to enhance osteogenesis and reduce osteoclastogenesis during fracture treatment[27,28]. The osteogenic effects of the GORoM hydrogel were explored using BMSCs cultured on the hydrogel surface. After 7 and 14 days of osteogenic induction, alkaline phosphatase (ALP) staining, alizarin red (ARS) staining, and mRNA expression (collagen type I [Col-1], osteocalcin [OCN], runt-related transcription factor 2 [RunX2], and osteopontin [OPN]) related to osteogenesis were assessed. The enzyme ALP, found on the surfaces of osteoblasts, is a widely acknowledged indicator of bone metabolism[29]. ALP staining and substantial ARS staining were observed across all hydrogel surfaces, with the GORoM hydrogel demonstrating more intense staining (Fig. 4A, B) and larger mineral nodules (Fig. 4C, D) on Days 7 and 14 than did those of the GO and GORo groups. This finding highlights the coordinated promotion of osteogenic differentiation by MBGNs and romosozumab in the GORoM hydrogel. These findings were corroborated by the mRNA expression levels of OPN, RunX2, OCN and Col-1 (Fig. 4E, F). Moreover, a similar trend was observed in the protein expression levels of OPN and RunX2, indicating an osteogenic synergistic effect from additional MBGNs and romosozumab (Fig. 4G–J). MBGN degradation releases Ca^{2+} and SiO_4^{4-}, which regulate stem cell osteogenic differentiation and bone formation[30,31]. The binding of romosozumab to sclerostin, an inhibitor of the Wnt/β-catenin signaling pathway, has been shown to enhance the survival of osteoblasts and osteocytes while reducing osteoclast occurrence[32]. This phenomenon occurs through an increase in osteoprotegerin (OPG) expression and a decrease in receptor activator of nuclear factor kappa-B ligand (RANKL) expression[33,34]. The specificity of romosozumab lies in its binding to sclerostin, a modulator of Wnt/β-catenin signaling. This interaction with sclerostin leads to the interaction of LRP5/6 and LRP4, effectively blocking Wnt binding to its receptor. This process involves coiled transmembrane receptor binding, GSK-3 phosphorylation by Zβ-catenin, and subsequent β-catenin degradation through ubiquitin-mediated proteolysis. This cascade ultimately promotes the expression of osteogenic genes[35]. In a comparison of the osteogenic effects of the GOM and GORoM hydrogels, several parameters, including ALP staining, ARS staining, mRNA expression (collagen type I [Col-1], osteocalcin

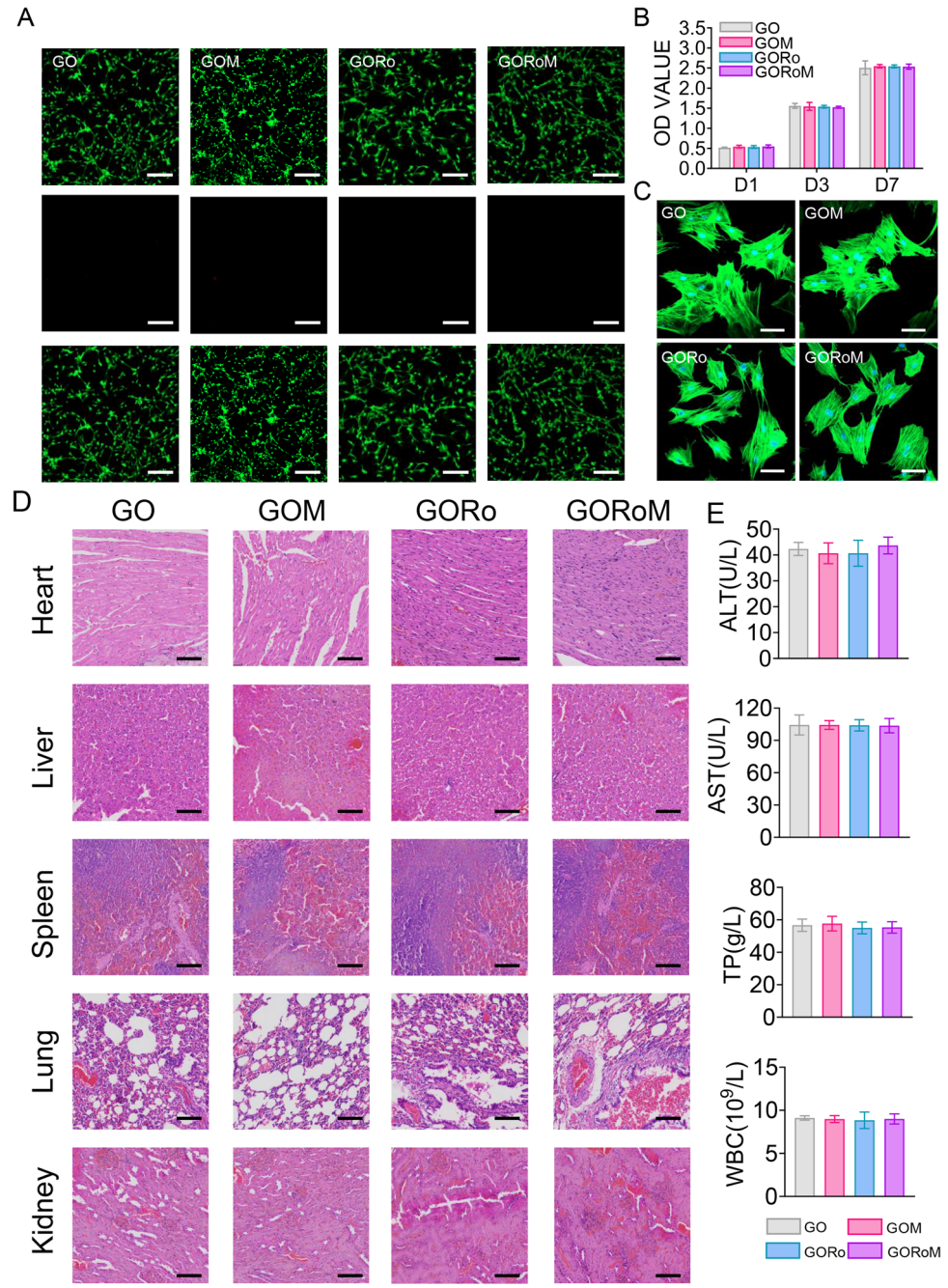

Fig. 3 In Vitro and In Vivo Biocompatibility of the GORoM Hydrogel. A Live/Dead staining of BMSCs after 24 h of coculture with different hydrogels. Live cells are marked with green fluorescence, and dead cells are marked with red fluorescence (scale bar: 200 μm). **B** CCK-8 assay results for BMSCs cultured on the hydrogels for 1, 3, and 7 days. **C** Cytoskeletal staining photos of cells cultured on the hydrogel after 2 days (scale bar: 50 μm). **D** Pathological images of the heart, liver, kidney, and lung of mice in each group (scale bar: 50 μm). **E** Serum levels of biomarkers reflecting liver and kidney function and blood cell parameters in the rats treated with the GORoM hydrogel ($n = 3$). *$p < 0.05$, **$p < 0.01$, and ***$p < 0.001$.

[OCN], Runt-related transcription factor 2 [RunX2], and osteopontin [OPN]), and protein expression (RunX2 and OPN), were notably elevated in the GORoM group. This trend was also observed for the quantitative analysis of ALP and ARS staining as well as for the assessment of osteogenic proteins (Fig. 4A–J). Collectively, these findings confirm that the beneficial in vitro osteogenic effects of both the GOM and GORoM hydrogels can be attributed to the sustained release of romosozumab through the utilization of MBGNs.

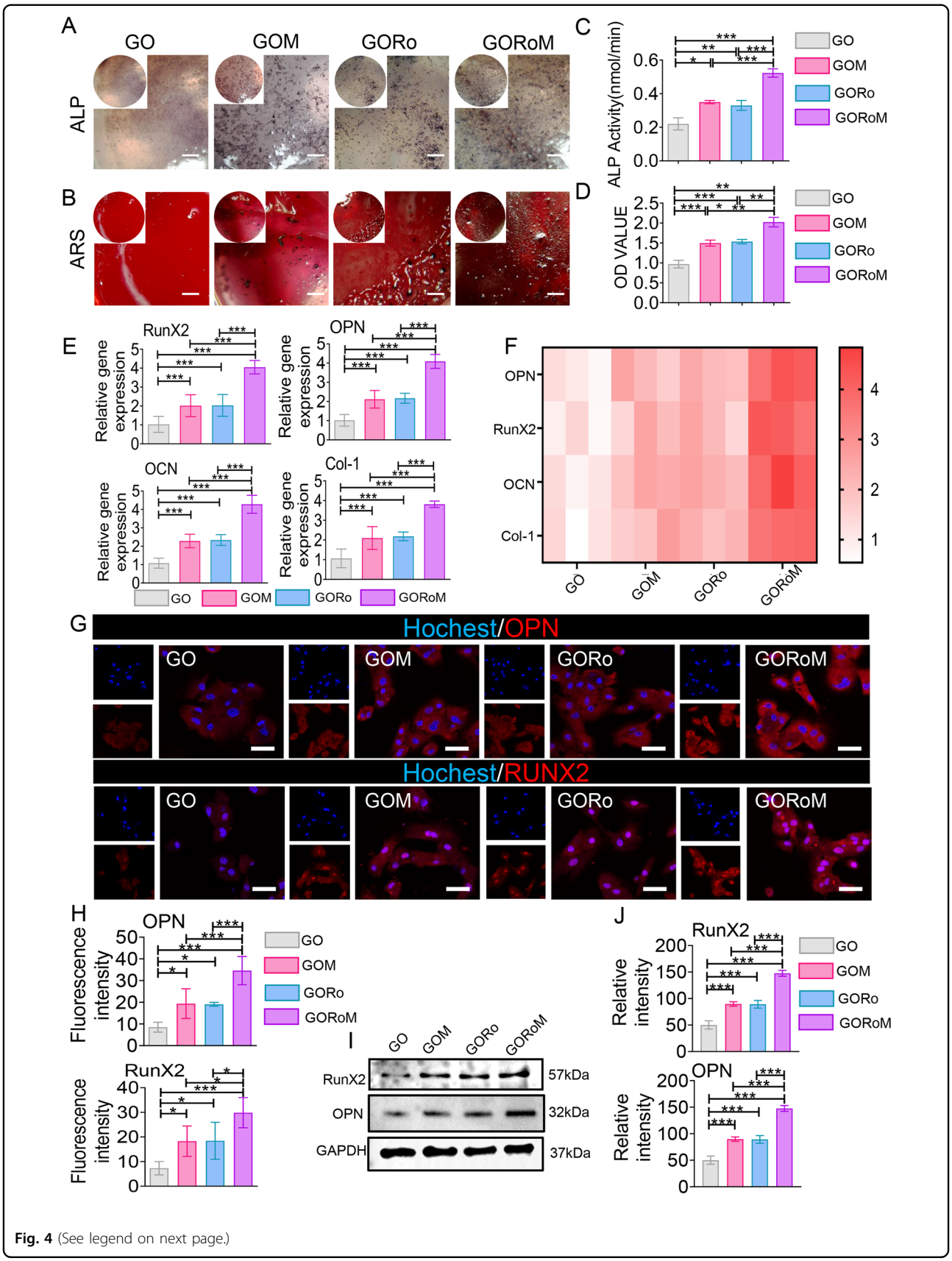

Fig. 4 (See legend on next page.)

(see figure on previous page)
Fig. 4 In vitro osteogenic differentiation-modulating property of the GMOS-based hydrogel. A ALP staining of BMSCs cultured on each adhesive for 7 days (scale bar: 100 μm). **B** ARS staining of BMSCs cultured on each adhesive for 14 days (scale bar: 100 μm). **C** Quantitative analysis of ALP staining ($n = 3$). **D** Quantitative analysis of ARS staining ($n = 3$). **E**, **F** The expression of osteogenesis-related genes, including OPN, RunX2, OCN, and Col-1, was estimated by RT–qPCR after BMSCs were cultured on the hydrogel surface for 14 days ($n = 3$). **G** Immunofluorescence images showing OPN and RunX2 staining of BMSCs cultured on the hydrogel surface for 14 days (scale bar: 50 μm). OPN and RunX2 were stained red, and the nuclei were stained blue. **H** Quantitative analysis of immunofluorescence staining ($n = 3$). **I** The protein expression of RunX2 and OPN was evaluated by Western blotting. **J** Quantitative analysis of the Western blotting data ($n = 3$). $^{*}p < 0.05$, $^{**}p < 0.01$, and $^{***}p < 0.001$.

The inhibitory effect of sample extracts on cell osteoclastic differentiation

We then explored how the hydrogels influenced osteoclast differentiation by employing BMDMs cultured in conditioned medium supplemented with osteoclast differentiation factors such as M-CSF and RANKL. RANKL, produced by osteocytes and osteoblasts, initiates the activation of the receptor activator of nuclear factor-B (RANK) on preosteoclasts, facilitating their transformation into mature osteoclasts[33]. TRAP staining was conducted on BMDMs following incubation with each GO-based adhesive to confirm the ability of each hydrogel to inhibit osteoclast formation. As shown in Fig. 5A, B, the GORo group displayed fewer TRAP-positive multinucleated cells after 7 days of culture than did the GO hydrogel group. Additionally, romosozumab resulted in a diminished actin ring size, indicating that romosuzumab significantly inhibited osteoclast maturation (Fig. 5C–E). As a result of the romosozumab-sclerostin interaction, Wnt/β-catenin signaling stimulates osteoblast and osteocyte survival, thereby inhibiting osteoclast maturation via enhanced OPG expression and reduced RANKL expression within osteoblasts and osteocytes[33]. Notably, GOM exhibited continuous romosuzumab release to prolong this effect, as the smallest TRAP-positive multinucleated cells and actin rings were observed in the GORoM group (Fig. 5A–E). Taken together, the above findings underscore the ability of our GORoM hydrogel to effectively suppress osteoclastic differentiation.

Assessment of bone formation and bone resorption in vivo

Prior in vivo findings underscore the dual capacity of the GORoM hydrogel to promote osteogenesis while inhibiting osteoclastogenesis, which is essential for restoring balanced bone formation (impacted by osteoblasts) and bone resorption (influenced by osteoclasts). Consequently, we sought to restore dysregulated bone homeostasis in vivo using an OVX rat model, a prevalent model in osteoporotic bone fracture studies[36–38]. After 12 weeks of ovariectomy-induced osteoporosis, a femur fracture rat model was established, and treatment involving the GO-based adhesive or no treatment was administered. At 6 and 12 weeks post-implantation, the rat femoral tissue was subjected to microcomputed tomography (micro-CT) analysis (Fig. 6A). The 3D-reconstructed images at 6 weeks exhibited no apparent fracture displacement across the three GO-based adhesive groups, indicating the ability of each adhesive to support early-stage fracture fixation. After 12 weeks, a fracture line could still be observed in the GO and GOM groups, while nearly complete fracture healing was evident in the GORoM group (Fig. 6B). Indicators such as bone mineral density (BMD), bone volume/tissue volume (BV/TV), and trabecular thickness (Tb.Th) improved throughout the 6-week period, indicating effective healing potential across all groups. At 12 weeks, the osteogenic indices (BMD, BV/TV, and Tb.Th) peaked in the GORoM group (Fig. 6C), highlighting the robust osteogenic effect of the GORoM hydrogel.

Then, decalcified histological sections underwent chemical (HE, Masson) and immunohistochemical staining, which included bone formation (Col-1, OCN) and resorption (TRAP)-related proteins to assess the regenerative process at the cellular and molecular levels. Consistent with the radiological findings, HE staining at 6 weeks revealed nonunion in all four groups (Fig. 7A). The GORoM group exhibited more newly synthesized collagen tissue (blue staining) at the fracture site, along with a heightened aggregation of osteoblasts. Consequently, new bone (red staining) formed along the edge of the bone defect (Fig. 7C). Masson staining revealed that the newly formed bone had evolved into a honeycomb-like trabecular bone structure at 12 + 6 weeks (Fig. 7B, D). Active osteoblasts clustered along the edge of the new bone, and the GORoM group exhibited no visible fracture line, accompanied by notable callus enlargement, indicating successful repair. During the evaluation of osteoblast and osteoclast activity, Col-1, a vital structural constituent of new bone tissue expressed during osteoblast differentiation, exhibited increased expression in newly grown trabecular bones in the GORoM group at both 6 and 12 weeks (Fig. 8A). Similarly, OCN (pivotal for staining osteoblasts and osteoids and expressed during bone

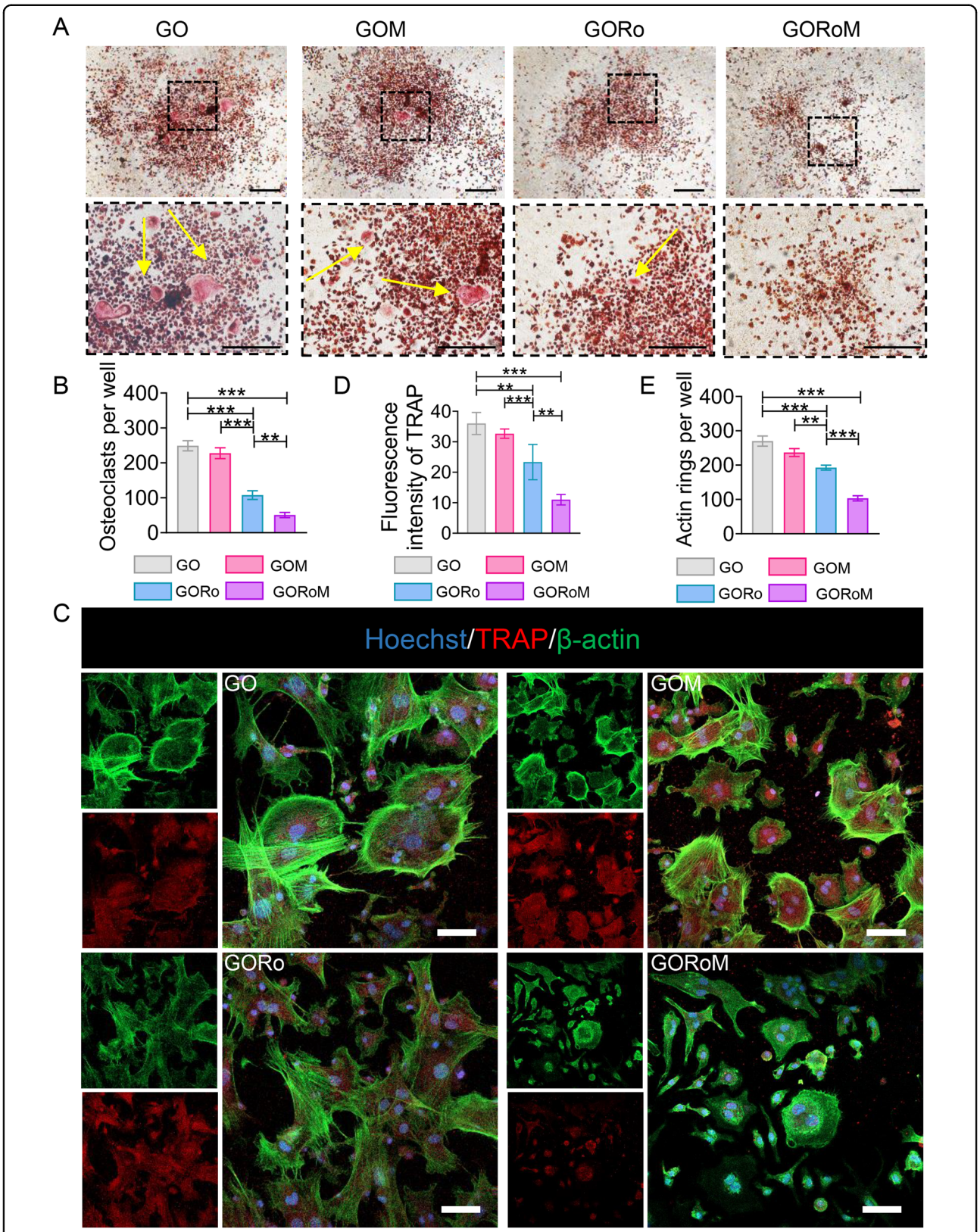

Fig. 5 Antiosteoclastic differentiation effect of the GORoM hydrogel on BMDMs. A TRAP staining of BMDMs cultured on different adhesive surfaces in RANKL-containing medium for 7 days (scale bar: 100 μm). **B** Quantitative analysis of TRAP-positive cells ($n = 3$). **C** Immunofluorescence staining for actin rings (green) and TRAP (red) on Day 7 (scale bar: 100 μm). **D** Quantitative analysis of the fluorescence intensity of TRAP ($n = 3$). **E** Quantitative analysis of the actin ring ($n = 3$). *$p < 0.05$, **$p < 0.01$, and ***$p < 0.001$.

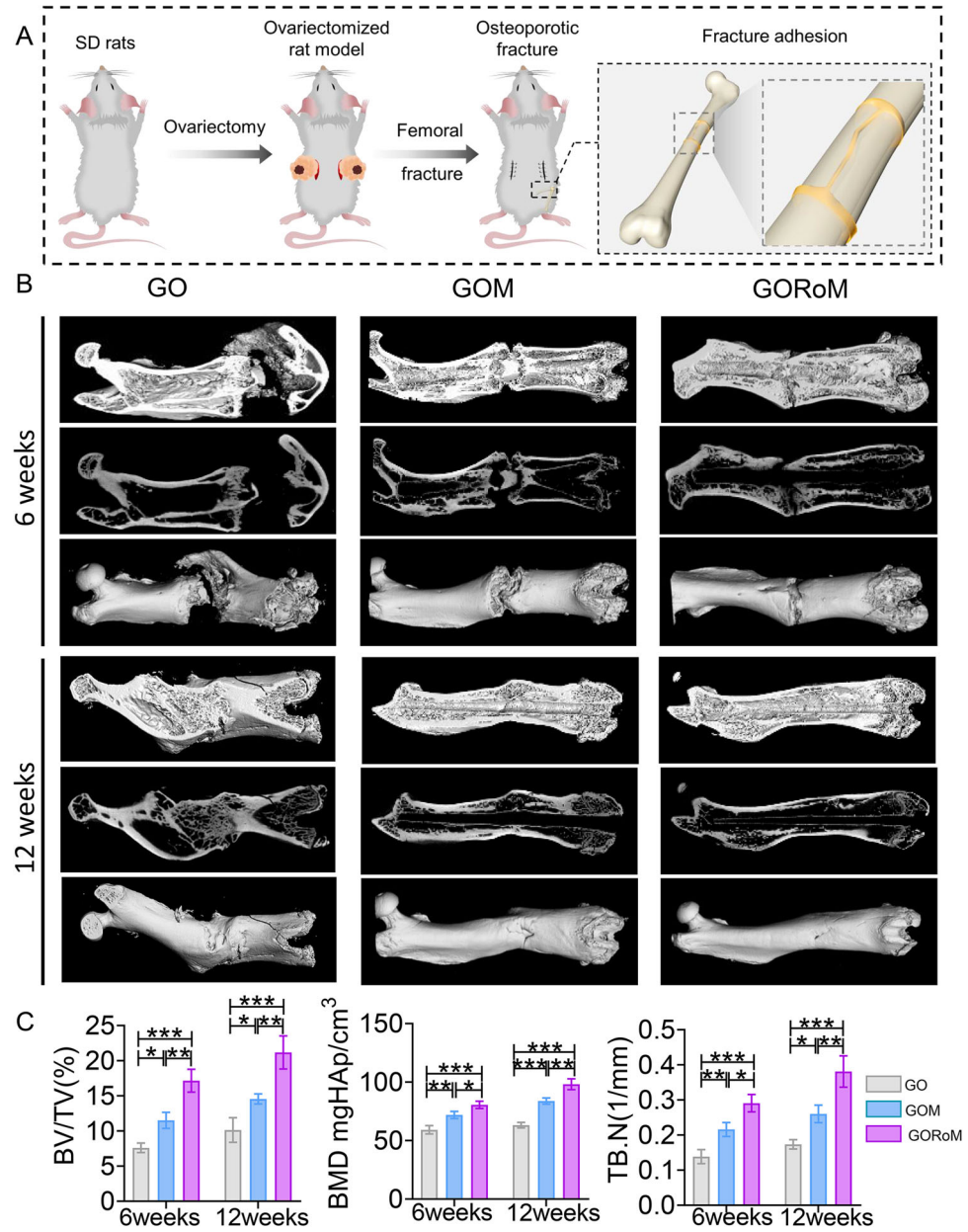

Fig. 6 In vivo osteoporotic bone regeneration by the GORoM hydrogel in an OVX rat femoral fracture model. A Schematic showing the OVX rat femoral fracture model and the therapeutic effect of the GORoM hydrogel on the OVX rat femoral fracture model. **B** Micro-CT 3D reconstruction of a rat femur at 6 and 12 weeks. **C** BV/TV, BMD, and Tb.N, which reflect the bone volume and mineral density in the defect region, were quantitatively analyzed ($n = 3$). *$p < 0.05$, **$p < 0.01$, and ***$p < 0.001$.

mineralization[39]) exhibited elevated expression in the GORoM group compared to the other two groups at 6 and 12 weeks (Fig. 8B). These results were further verified by quantitative analysis (Fig. 8C). Importantly, TRAP staining and quantitative analysis (Fig. 9A, B) revealed numerous RANKL-positive osteoclasts (claret-stained) at the fracture site in the GO group, while no osteoclasts were observed in the GORoM group. These findings confirm the ability of GORoM to suppress osteoclast activity and effectively reverse bone loss in OVX rats.

In summary, the GORoM hydrogel adopts a multi-faceted approach to promote osteoporotic fracture regeneration by combining fracture fixation with rebalancing the bone remodeling process to strengthen osteogenesis while dampening bone resorption activity to achieve comprehensive osteoporotic fracture regeneration.

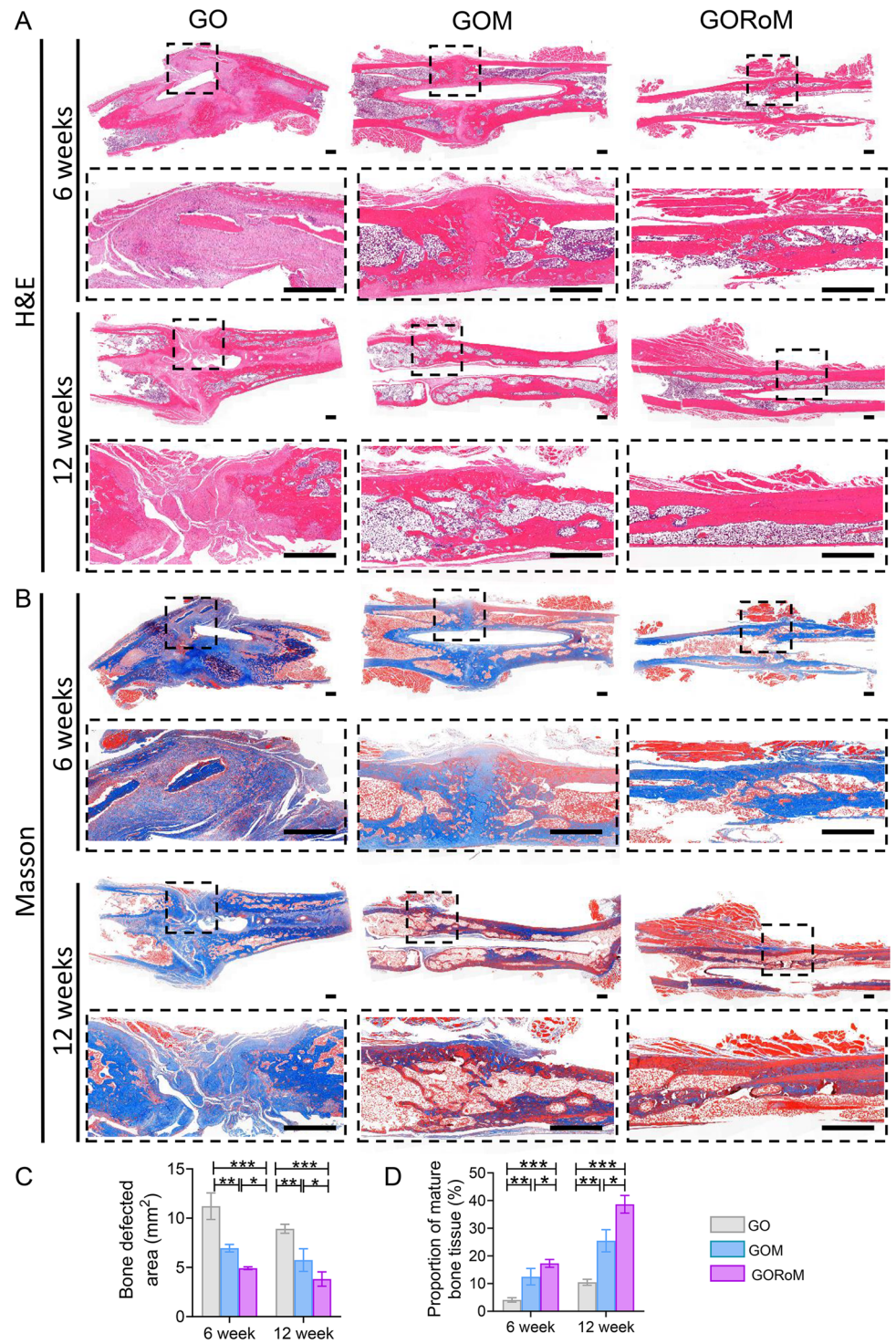

Fig. 7 Histological analysis of the bone tissue in decalcified sections at 6 and 12 weeks. A HE staining and **B** Masson staining of defect areas after 6 and 12 weeks of treatment at low and high magnifications, respectively (scale bar: 500 μm). **C** Quantitative analysis of the bone defect area after 6 and 12 weeks ($n = 3$). **D** The quantitative proportion of mature bone tissue (stained with red) after 6 and 12 weeks ($n = 3$). *$p < 0.05$, **$p < 0.01$, and ***$p < 0.001$.

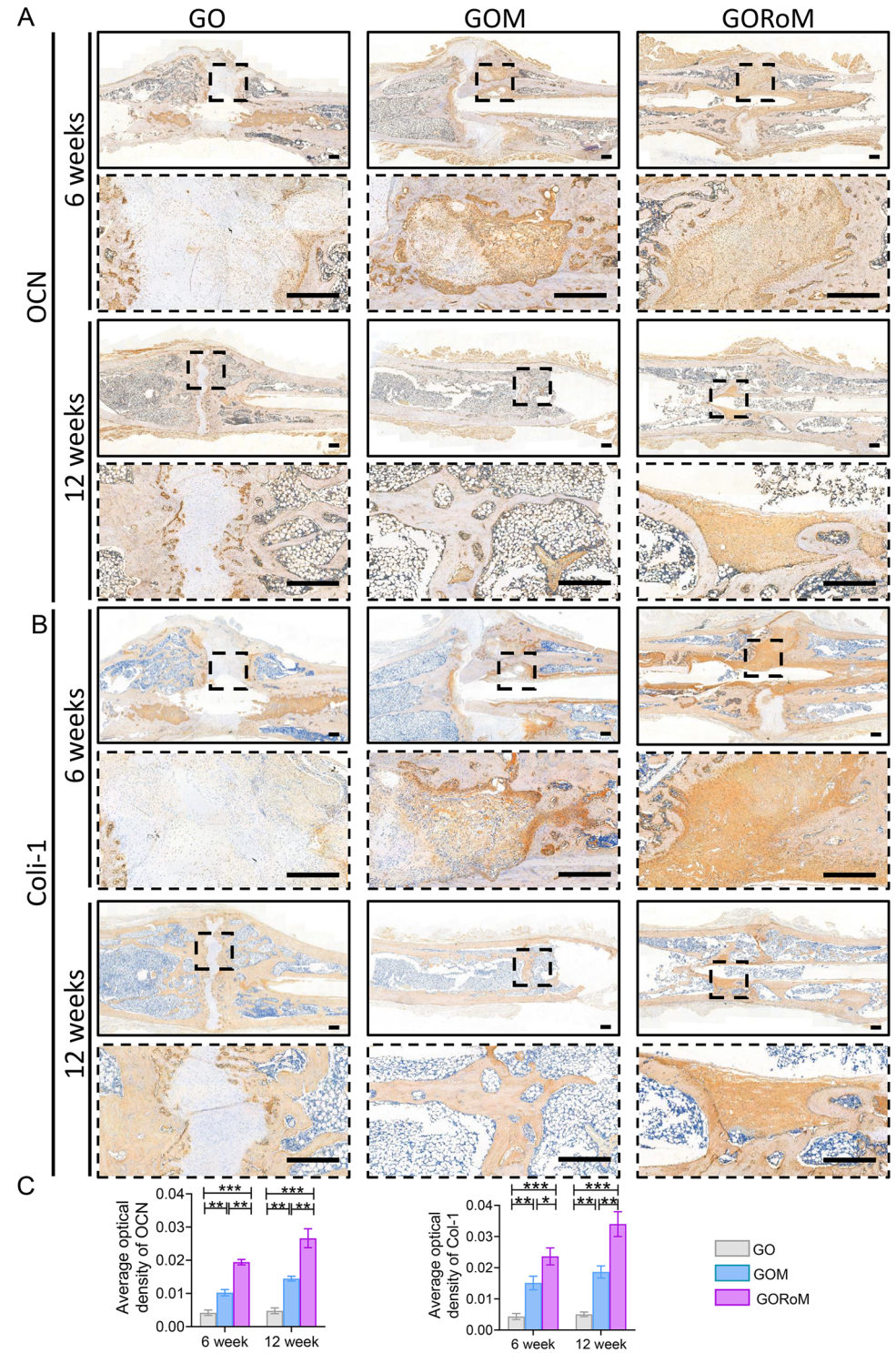

Fig. 8 Histological analysis of osteogenic activity. A Immunohistochemical staining of OCN in bone defects at 6 and 12 weeks (scale bar: 500 μm). **B** Immunohistochemical staining of Col-1 in bone defects at 6 and 12 weeks (scale bar: 500 μm). **C** Quantitative analysis of OCN and Col-1 expression at 6 and 12 weeks ($n = 3$). *$p < 0.05$, **$p < 0.01$, and ***$p < 0.001$.

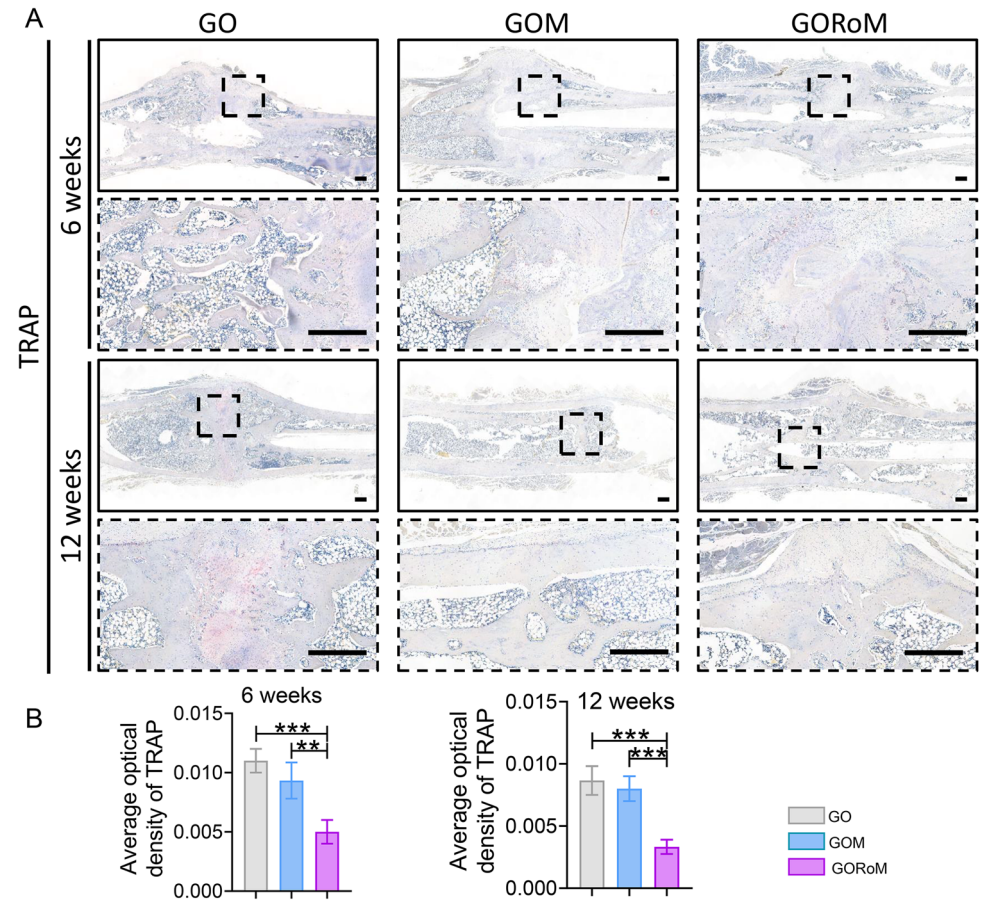

Fig. 9 Histological analysis of osteoclastogenesis. A Immunohistochemical staining of TRAP (scale bar: 500 μm). **B** Quantitative analysis of TRAP staining at 6 and 12 weeks ($n = 3$). *$p < 0.05$, **$p < 0.01$, and ***$p < 0.001$.

Conclusion

Our multifunctional biodegradable orthopedic adhesive can mend fracture fragments and restore bone homeostasis, exhibiting pro-osteogenic and anti-osteoclastogenic properties. Leveraging intermolecular hydrogen bonds and dynamic covalent Schiff base networks, these partially crosslinked hydrogels demonstrate remarkable adaptability in complex clinical situations, featuring attributes such as injectability and reversible adhesion. The adhesive's mechanical robustness is enhanced upon full crosslinking, and the adhesive firmly adheres to isolated porcine bone fragments. The exceptional biocompatibility of these hydrogels underscores their efficacy in promoting bone tissue regeneration. Our research extended to a rat model of femur fracture and osteoporosis induced by ovariectomy, revealing the impact of the adhesive on fracture healing. The released MBGNs (micro/nanosized bioactive glass particles) and romosozumab play crucial roles in orchestrating fracture healing within the context of osteoporosis. Romosozumab, when released from MBGNs, accelerates osteogenic processes while simultaneously inhibiting osteoclast formation. This dual approach addresses osteoporotic pathology, corrects abnormal bone remodeling, and stimulates regeneration. As a result, our GORoM hydrogel is an orthopedic adhesive that enhances fracture fixation and coordinates an improved bone integration process. This hydrogel inhibits osteoclast formation, ultimately expediting the healing of osteoporotic fractures.

Acknowledgements

This work was supported by the President Foundation of Nanfang Hospital, Southern Medical University (No. 2020C023), the Science and Technology Planning Project of Guangzhou, China (No. 2023A04J2316), the Natural Science Foundation of Fujian Province (No. 2021J011156), the National Natural Science Foundation of China (No. 22176080) and the Natural Science Foundation of Shandong Province (No. ZR2023YQ015).

Author details

[1]Department of Orthopaedics, Ningde Municipal Hospital of Ningde Normal University, Ningde 352100, China. [2]Division of Orthopaedic Surgery, Department of Orthopaedics, Nanfang Hospital, Southern Medical University, Guangzhou 510515, China. [3]Jiangxi Provincial People's Hospital, The First Affiliated Hospital of Nanchang Medical College, Nanchang 330006, China.

[4]Division of Orthopaedics and Traumatology, Department of Orthopaedics, Nanfang Hospital, Southern Medical University, Guangzhou 510515, China. [5]Key Laboratory of Interfacial Reaction & Sensing Analysis in Universities of Shandong, School of Chemistry and Chemical Engineering, University of Jinan, Jinan 250022, China. [6]Department of Orthopaedics, Guangzhou First People's Hospital, South China University of Technology, Guangzhou 510180, China

Author contributions

W.L., K.C. and Z.F.G. conceived the idea and designed the experiment. S.S. and J.X. conducted the experiments and data analysis. S.S. wrote the manuscript. J.G., J.L., X.D. and S.L. assisted with the writing of the manuscript.

Data availability

The data will be made available upon request.

Conflict of interest

The authors declare no competing interests.

Ethics

Animal research at South China Agricultural University was conducted with the approval of the university's Animal Ethics Committee. All animal experiments followed the National Institutes of Health (NIH) Guidelines for the Care and Use of Laboratory Animals.

Publisher's note

Springer Nature remains neutral with regard to jurisdictional claims in published maps and institutional affiliations.

Supplementary information The online version contains supplementary material available at https://doi.org/10.1038/s41427-024-00539-7.

Received: 30 November 2023 Revised: 27 January 2024 Accepted: 29 January 2024.
Published online: 12 April 2024

References

1. Hernlund, E. et al. Osteoporosis in the European Union: medical management, epidemiology and economic burden. *Arch. Osteoporos.* **8**, 136 (2013).
2. Si, L., Winzenberg, T. M., Jiang, Q., Chen, M. & Palmer, A. J. Projection of osteoporosis-related fractures and costs in China: 2010–2050. *Osteoporosis Int.* **26**, 1929–1937 (2015).
3. Song, S., Guo, Y., Yang, Y. & Fu, D. Advances in pathogenesis and therapeutic strategies for osteoporosis. *Pharmacol. Ther.* **237**, 108168 (2022).
4. Ferrari, S. et al. Unmet needs and current and future approaches for osteoporotic patients at high risk of hip fracture. *Arch. Osteoporos.* **11**, 37 (2016).
5. Jain, J. P., Modi, S., Domb, A. J. & Kumar, N. Role of polyanhydrides as localized drug carriers. *J. Control. Rel.* **103**, 541–563 (2005).
6. Zhao, Y. et al. Bioinspired mineral hydrogels as nanocomposite scaffolds for the promotion of osteogenic marker expression and the induction of bone regeneration in osteoporosis. *Acta Biomater.* **113**, 614–626 (2020).
7. Yang, Y. et al. Triple-functional bone adhesive with enhanced internal fixation, bacteriostasis and osteoinductive properties for open fracture repair. *Bioact. Mater.* **25**, 273–290 (2023).
8. Guan, P. et al. Exosome-loaded extracellular matrix-mimic hydrogel with anti-inflammatory property facilitates/promotes growth plate injury repair. *Bioact. Mater.* **10**, 145–158 (2022).
9. Cui, C. et al. Water-triggered hyperbranched polymer universal adhesives: From strong underwater adhesion to rapid sealing hemostasis. *Adv. Mater.* **31**, 1905761 (2019).
10. Zhao, Y. et al. Supramolecular adhesive hydrogels for tissue engineering applications. *Chem. Rev.* **122**, 5604–5640 (2022).
11. Xu, L. et al. Bioactive pore-forming bone adhesives facilitating cell ingrowth for fracture healing. *Adv. Mater.* **32**, 1907491 (2020).
12. Hasani-Sadrabadi, M. M. et al. An engineered cell-laden adhesive hydrogel promotes craniofacial bone tissue regeneration in rats. *Sci. Transl. Med.* **12**, eaay6853 (2020).
13. Yang, Q. et al. Exosomes-loaded electroconductive nerve dressing for nerve regeneration and pain relief against diabetic peripheral nerve injury. *Bioact. Mater.* **26**, 194–215 (2023).
14. Steffi, C., Shi, Z., Kong, C. H. & Wang, W. Modulation of osteoclast interactions with orthopaedic biomaterials. *J. Func. Biomater.* **9**, 18 (2018).
15. Kammerlander, C., Erhart, S., Doshi, H., Gosch, M. & Blauth, M. Principles of osteoporotic fracture treatment. *Best Pract. Res. Clin. Rheumatol.* **27**, 757–769 (2013).
16. Maeda, K. et al. The regulation of bone metabolism and disorders by wnt signaling. *Int. J. Mol. Sci.* **20**, 5525 (2019).
17. Delgado-Calle, J., Sato, A. Y. & Bellido, T. Role and mechanism of action of sclerostin in bone. *Bone* **96**, 29–37 (2017).
18. Suen, P. K. & Qin, L. Sclerostin, an emerging therapeutic target for treating osteoporosis and osteoporotic fracture: A general review. *J. Orthop. Transl.* **4**, 1–13 (2016).
19. Holdsworth, G., Roberts, S. J. & Ke, H. Z. Novel actions of sclerostin on bone. *J. Mol. Endocrinol.* **62**, R167–R185 (2019).
20. Liu, S. et al. Non-coding-RNA-activated core/chitosan shell nanounits coated with polyetheretherketone for promoting bone regeneration and osseointegration via osteoimmunology. *ACS Appl. Mater. Interfaces* **15**, 12653–12668 (2023).
21. Zhou, L. et al. Hybrid gelatin/oxidized chondroitin sulfate hydrogels incorporating bioactive glass nanoparticles with enhanced mechanical properties, mineralization, and osteogenic differentiation. *Bioact. Mater.* **6**, 890–904 (2021).
22. Fan, L. et al. Exosomes-loaded electroconductive hydrogel synergistically promotes tissue repair after spinal cord injury via immunoregulation and enhancement of myelinated axon growth. *Adv. Sci.* **9**, 2105586 (2022).
23. Liang, F. et al. Ropivacaine microsphere-loaded electroconductive nerve dressings for long-acting analgesia and functional recovery following diabetic peripheral nerve injury. *Mater. Today Bio* **21**, 100712 (2023).
24. Tian, Y. et al. Strong Biopolymer-based nanocomposite hydrogel adhesives with removability and reusability for damaged tissue closure and healing. *ACS Appl. Mater. Interfaces* **14**, 54488–54499 (2022).
25. El-Fiqi, A., Kim, J.-H. & Kim, H.-W. Osteoinductive fibrous scaffolds of biopolymer/mesoporous bioactive glass nanocarriers with excellent bioactivity and long-term delivery of osteogenic drug. *ACS Appl. Mater. Interfaces* **7**, 1140–1152 (2015).
26. Hou, F. et al. Biodegradable dual-crosslinked adhesive glue for fixation and promotion of osteogenesis. *Chem. Eng. J.* **427**, 132000 (2022).
27. Kenkre, J. S. & Bassett, J. H. D. The bone remodelling cycle. *Ann. Clin. Biochem.* **55**, 308–327 (2018).
28. Florencio-Silva, R., Sasso, G. R. D. S., Sasso-Cerri, E., Simoes, M. J. & Cerri, P. S. Biology of bone tissue: structure, function, and factors that influence bone cells. *Biomed Res. Int.* **2015**, 421746 (2015).
29. Vimalraj, S. Alkaline phosphatase: Structure, expression and its function in bone mineralization. *Gene* **754**, 144855 (2020).
30. Xin, T. et al. Inorganic strengthened hydrogel membrane as regenerative periosteum. *ACS Appl. Mater. Interfaces* **9**, 41168–41180 (2017).
31. Patel, K. D. et al. Combined effects of nanoroughness and ions produced by electrodeposition of mesoporous bioglass nanoparticle for bone regeneration. *ACS Appl. Bio Mater.* **2**, 5190–5203 (2019).
32. McClung, M. R. et al. Romosozumab in postmenopausal women with low bone mineral density. *N. Engl. J. Med.* **370**, 412–420 (2014).
33. Udagawa, N. et al. Osteoclast differentiation by RANKL and OPG signaling pathways. *J. Bone Miner. Metab.* **39**, 19–26 (2021).
34. Tella, S. H. & Gallagher, J. C. Prevention and treatment of postmenopausal osteoporosis. *J. Steroid Biochem. Mol. Biol.* **142**, 155–170 (2014).
35. Brommage, R. Genetic approaches to identifying novel osteoporosis drug targets. *J. Cell. Biochem.* **116**, 2139–2145 (2015).
36. Qi, X. et al. Exosomes secreted by human-induced pluripotent stem cell-derived mesenchymal stem cells repair critical-sized bone defects through enhanced angiogenesis and osteogenesis in osteoporotic rats. *J. Cell. Biochem.* **12**, 836–849 (2016).
37. Li, H. et al. Lutein Suppresses oxidative stress and inflammation by nrf2 activation in an osteoporosis rat model. *Med. Sci. Monitor.* **24**, 5071–5075 (2018).
38. Du, M. et al. Effect of Dihuang rougui decoction on ovariectomy-induced osteoporosis in rats. *Trop. J. Pharm. Res.* **17**, 423–427 (2018).
39. Dutta, S. D., Hexiu, J., Patel, D. K., Ganguly, K. & Lim, K.-T. 3D-printed bioactive and biodegradable hydrogel scaffolds of alginate/gelatin/cellulose nanocrystals for tissue engineering. *Int. J. Biol. Macromol.* **167**, 644–658 (2021).